JACS
JOURNAL OF THE AMERICAN CHEMICAL SOCIETY
Article
pubs.acs.org/JACS

Multitemplates for the Hierarchical Synthesis of Diverse Inorganic Materials

Zhenfeng Bian,[†] Jian Zhu,[†] Jinguo Wang,[†] Shengxiong Xiao,[‡] Colin Nuckolls,*[,‡] and Hexing Li*[,†]

[†]The Education Ministry Key Laboratory of Resource Chemistry, Shanghai Key Laboratory of Rare Earth Functional Materials, Shanghai Normal University, Shanghai 200234, China

[‡]Department of Chemistry, Columbia University, New York, New York 10027, United States

Supporting Information

ABSTRACT: Described here is a new and highly general strategy for multiple-template (multitemplate) patterning. This process is significant because it allows us to create various unusual shapes such as solid spheres, yolk–shell spheres, flowerlike particles, and structured nanocomponents. Alcoholysis of the metal–organic precursors with mixtures of glycerol and various amounts of ethanol followed by calcination yields oxides. The glycerol plays the dual role of hierarchically assembling the metal–organic composites and stabilizing the structures during the subsequent conversions. Furthermore, we demonstrate for the first time that these metal–organic composites can be converted into oxides, nitrides, and highly graphitized carbon nanostructures. We show that these yolk–shell structures display superior photocatalytic activity and electrochemical properties.

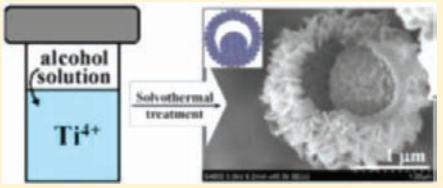

INTRODUCTION

Diverse molecular architectures with fascinating properties have inspired the design of intricate artificial nanostructures.[1−3] To date, a great number of inorganic materials with tunable structures have been synthesized by one-to-one templation from "guest" to "host".[4−16] The development of a simple method for preparing structurally and functionally diverse materials would be highly desirable because would provide broad applicability. Solvothermal alcoholysis has received a large amount of interest in regard to creating metal oxides because of the control over the particle size, shape, and crystal structure that it provides.[17,18] The alcoholysis of Ti^{4+} shown below produces TiO_2, where the oxygen in the oxide originates come from the alcohol:

$$TiX_4 + 4R{-}OH \rightarrow Ti(OR)_4 + 4HX$$

$$Ti(OR)_4 + TiX_4 \rightarrow 2TiO_2 + 4RX$$

The TiO_2 then nucleates into a crystal. The majority of studies involving preparation of nanoparticles from TiO_2 have utilized monohydroxyl alcohols that have highly stabilized carbocations, such as benzyl alcohol and *tert*-butanol.[19] After nucleation, the organic species resulting from alcoholysis is removed, affording the pure metal oxides. Here we explore the idea of how molecules with multiple hydroxyl functionalities (e.g., glycerol) affect this process. Remarkably, under these conditions, we are able to create a diversity of new nanomaterials with unusual shapes. In addition, these materials have higher content of organic material incorporated into them and can form metal–organic composites that can be used as templates to yield hierarchical nanostructures.

RESULTS AND DISCUSSION

Nanoscale plates of TiO_2 form when $TiOSO_4$ reacts with glycerol. We were unsuccessful in isolating the adduct between glycerol and $TiOSO_4$. The nanoscale plates are shown in Figure 1. We call these plates "nanotechtons". The selected-area electron diffraction (SAED) pattern (Figure 1c inset) reveals that the nanotechtons are amorphous. From the side view of the transmission electron microscopy (TEM) image (Figure 1b inset), it is interesting to note that such nanotechtons then stack into multilayers via a self-assembly process. When another alcohol (e.g., ethanol, propanol, isopropanol, *n*-butanol, *tert*-butanol, or benzyl alcohol) is used in place of glycerol, we obtain solid spheres of TiO_2 (Figure S1 in the Supporting Information). These spherical samples have been prepared previously from the random aggregation of TiO_2 particles.[20] In general, the orientation growth of nanocrystals has been applied to explain the formation of such structures.[21,22]

The scheme for the formation of these nanotechtons is shown in Figure 1d. The final reaction to form the network depends on the in situ-produced water from the condensation of glycerol. This dehydration reaction was confirmed by gas chromatography–mass spectrometry (GC–MS) studies. These studies showed the formation of ethers from glycerol or ethanol (Figure S2). Upon further solvothermolysis, H_2O is produced in situ and induces the subsequent hydrolysis and assembly of titanium alkoxide groups. The slow release of the water affords the time for self-assembly to occur.

Unlike monofunctional alcohols, glycerol has three hydroxyl groups per molecule. The alcoholysis products interconnect through unreacted hydroxyl groups that engage in hydrogen

Received: November 1, 2011
Published: January 3, 2012

   dx.doi.org/10.1021/ja210270m | *J. Am. Chem.Soc.* 2012, 134, 2325–2331

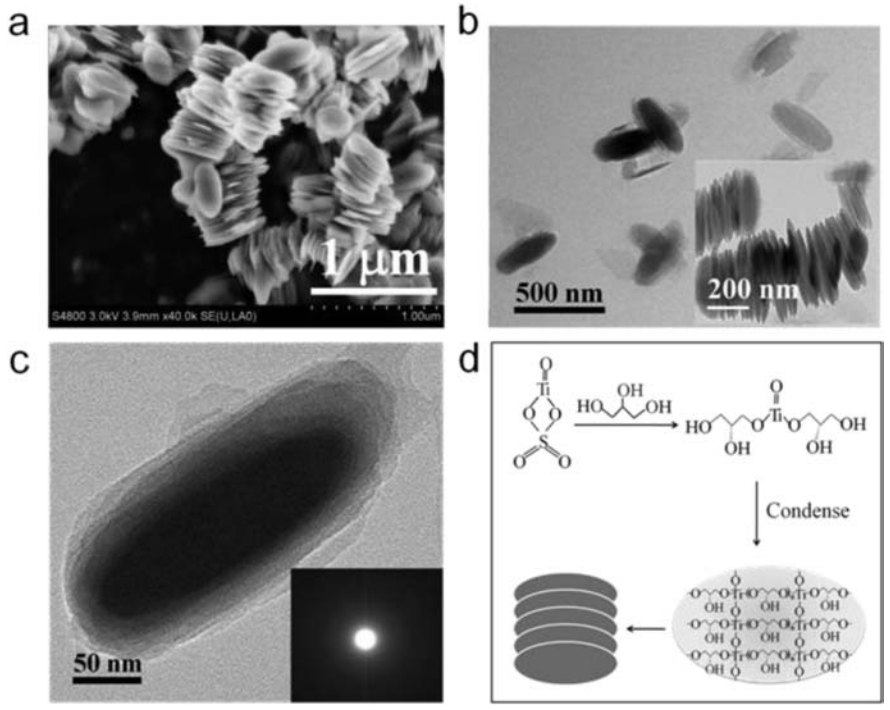

Figure 1. Nanotechtons formed from TiO_2. (a) SEM image. (b, c) TEM images. The inset of (b) is a side view of the sample, and (c) is a top view of the sample. The inset of (c) is a SAED pattern. (d) Schematic illustration of the formation of nanotechtons.

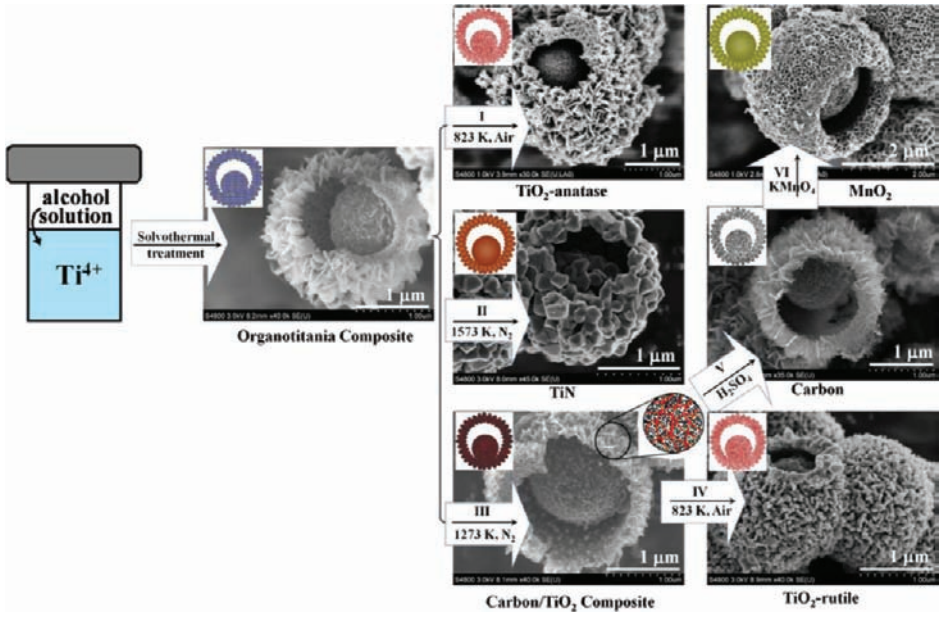

Figure 2. Images showing the conversion of the yolk−shell organotitania composite (left) into nanostructured (I) anatase TiO_2; (II) TiN; (III) carbon/TiO_2 composite; (IV) rutile TiO_2; (V) graphitized carbon; and (VI) MnO_2.

bonds to form a 2D nanostructure (Figure 1d). In the Fourier transform IR (FTIR) spectrum (Figure S3), we observed resonances at 2880 and 2938 cm^{-1}, corresponding to the C−H structure of glycerol, and peaks between 1000 and 1200 cm^{-1}, corresponding to the C−O structure of glycerol; the absorption peaks at 3408 and 1640 cm^{-1} can be assigned to the OH functionality. Moreover, the broad peak at 3408 cm^{-1} results from hydrogen bonds in the nanotechton network sample.[23] As a result of the existence of the hydrogen bonds, the formed 2D nanopieces are arranged into an ordered lamellar structure. Energy-dispersive X-ray (EDX) analysis of the nanotechtons (Table S1 in the Supporting Information) revealed a higher content of carbon in the form of organics when polyfunctional alcohols are used as reagents. These organics and Ti−OH fragments block the crystal growth of TiO_2.

In contrast, monofunctional alcohols such as ethanol react with $TiOSO_4$ to form $O{=}Ti(OR)_2$. The −OR group can readily be replaced by a hydroxyl group from water. Because of the random aggregation of Ti−OH, spherical particles result. To probe further the importance of the three hydroxyl groups in the formation of the nanotechtons, we replaced the glycerol with ethylene glycol. After reaction for 2 days between ethylene

dx.doi.org/10.1021/ja210270m | J. Am. Chem.Soc. 2012, 134, 2325−2331

glycol and titanium sulfate, no lamellar structure could be seen; we observed only irregularly shaped clusters (Figure S4). We thus conclude that the middle hydroxyl of the glycerol molecule is vitally important in the formation of the nanotechtons. As further support for the importance of the third hydroxyl in glycerol, we did not obtain any lamellar structures in reactions between $TiOSO_4$ and ethylene glycol. Additionally, reaction of 1,2-propanediol or 1,3-propanediol with $TiOSO_4$ gave no solid.

The structure of the organotitania composites can be tuned in the solvothermal alcoholysis reaction by varying the ratio of glycerol to ethanol and the time of the reaction. The results are collected in Table S2 and shown in Figure S5. Solid spheres, yolk–shell spheres, and hollow spheres were obtained in the solvothermal alcoholysis of $TiOSO_4$ in mixtures of ethanol and glycerol reacted for 1, 48, and 336 h, respectively. The solid spheres may be attributed to the alcoholysis of $TiOSO_4$ with ethanol, since no solid products can be collected even after solvothermal alcoholysis of $TiOSO_4$ with glycerol alone for 5 h. The presence of glycerol promotes the aggregation, leading to bigger spheres than observed when pure ethanol is used (Figure S6). With a prolonged solvothermal reaction time (48 h), both nanotechtons (from glycerol) and solid spheres (from ethanol) result from alcoholysis with $TiOSO_4$. These nanotechtons then assemble around the solid spheres [see the model and scanning electron microscopy (SEM) images in Figures S5 and S7, respectively], after which stepwise alcoholysis and a Kirkendall process occur.[24,25] This process produces the yolk–shell spheres. The yolk in the yolk–shell spheres continuously shrinks over time, creating hollow spheres after 336 h of reaction (Figure S7). In contrast, when $TiCl_4$ was used instead of $TiOSO_4$, flowerlike particles were obtained. These flowerlike structures result from the very tiny particles produced by alcoholysis of $TiCl_4$ with ethanol, since chloride ions inhibit particle agglomeration.[20] The flowerlike particles are too small to be seen clearly after being covered with the nanotechtons produced by alcoholysis of $TiCl_4$ with glycerol (Figure S5).

In addition to organizing the organotitania composites, the glycerol also greatly enhances the content of organic species in the composites. Table S3 contains the carbon content for various preparations. The high content of the organic species plays a crucial role in stabilizing the structure of organotitania composites and thus allowing the subsequent transformations. Figure 2 illustrates the unique template conversion process of yolk–shell organotitania composites (Figure 2left) into structurally and functionally diverse TiO_2, TiN, carbon/TiO_2 composite, carbon, and MnO_2 (Figure 2I–VI). Calcination at 823 K in air (step I) results in yolk–shell TiO_2 spheres (Figure 2b). The TiO_2 is exclusively in the anatase phase and has high crystallinity (Figure S8a). Moreover, these materials have a mesoporous structure with high surface area, as determined from N_2 adsorption–desorption curves (Figure S8b and Table S4).

Alternatively, we obtain yolk–shell TiN by calcination under N_2 at 1573 K (step II in Figure 2). Figure S9 displays the X-ray diffraction (XRD) pattern for this material. Less than 1.0 mol % carbon could be detected by EDX analysis (Figure S10). We propose that the carbon species in the initial organotitania composite were removed from the Ti–O bonds as CO_2. This also explains the formation of TiN at relatively low temperatures.[26] Importantly, this new approach to the synthesis of TiN affords a nanostructure with high surface area (see Table S5). These two properties are conducive to the application of TiN as a catalyst or a support for a catalytic structure.[26,27] Few synthetic methods can simultaneously control the nanostructure while achieving high surface area.[27]

Calcination of organotitania composites under N_2 atmosphere at lower temperature (1273 K; step III in Figure 2) does not form TiN. The XRD patterns display only the rutile phase of TiO_2 (Figure S9). The carbon and TiO_2 species are homogeneously distributed in the yolk–shell carbon/TiO_2 composite (Figure 2 and Figure S8). This can be visualized directly in the mapping images (Figure S11). These cross-linked carbon and TiO_2 species are able to stabilize the original structures, which are subsequently transformed into yolk–shell TiO_2 by calcination in air at 823 K to remove the carbon (step IV in Figure 2). Unlike the TiO_2 obtained by direct calcination of the organotitania composite at 823 K, the TiO_2 resulting from calcination of the carbon/TiO_2 composite displays a pure rutile phase (see the XRD pattern in Figure S12) as a result of the transformation from the anatase phase at high temperature (see the XRD patterns in Figure S9). Alternatively, etching the carbon/TiO_2 composite with 98 wt % H_2SO_4 solution removes TiO_2 and gives rise to the yolk–shell carbon system instead (step V in Figure 2).

The high-resolution TEM (HRTEM) image and SAED pattern (Figure 3a) reveal that the yolk–shell carbon obtained

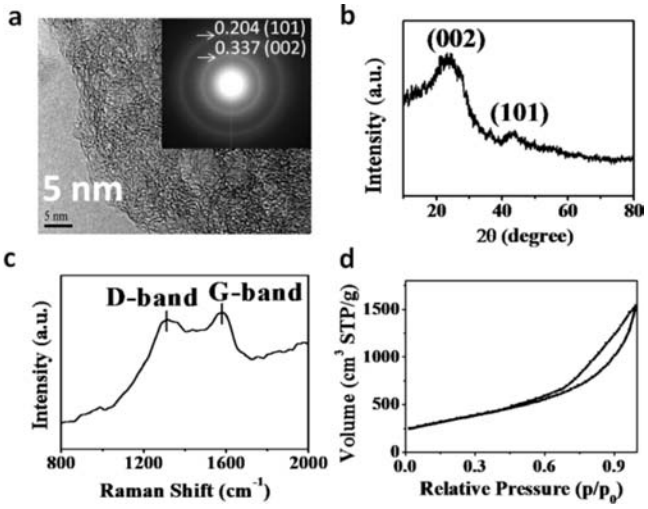

Figure 3. Graphitization and mesoporous features of yolk–shell carbon. (a) HRTEM image. The inset is the SAED pattern. (b) XRD pattern. (c) Raman spectrum. (d) N_2 adsorption–desorption isotherm.

from the carbon/TiO_2 composite exhibits graphitic features that are confirmed by the XRD pattern (Figure 3b).[28,29] Meanwhile, the Raman spectrum (Figure 3c) displays two bands around 1580 and 1340 cm^{-1}. These resonances are indicative of graphitized carbon (G band) and amorphous carbon (D band), respectively.[30] However, the carbon atoms in the frameworks with randomly distributed graphitic layers exhibit weak XRD reflections and less defined Raman signatures. This graphitization process of the yolk–shell structure was also performed at temperatures ranging from 500 to 1000 °C and probed using Raman spectroscopy (Figure S13). With increasing calcination temperature, the ratio (I_D/I_G) decreases slightly, indicating the enhancement of the graphitization process. TiO_2 catalysis causes the graphitic features;[31] TiO_2 is known to promote graphitization at low temperature, similar to what was observed in Fe_2O_3 catalysis.[32]

dx.doi.org/10.1021/ja210270m | J. Am. Chem.Soc. 2012, 134, 2325–2331

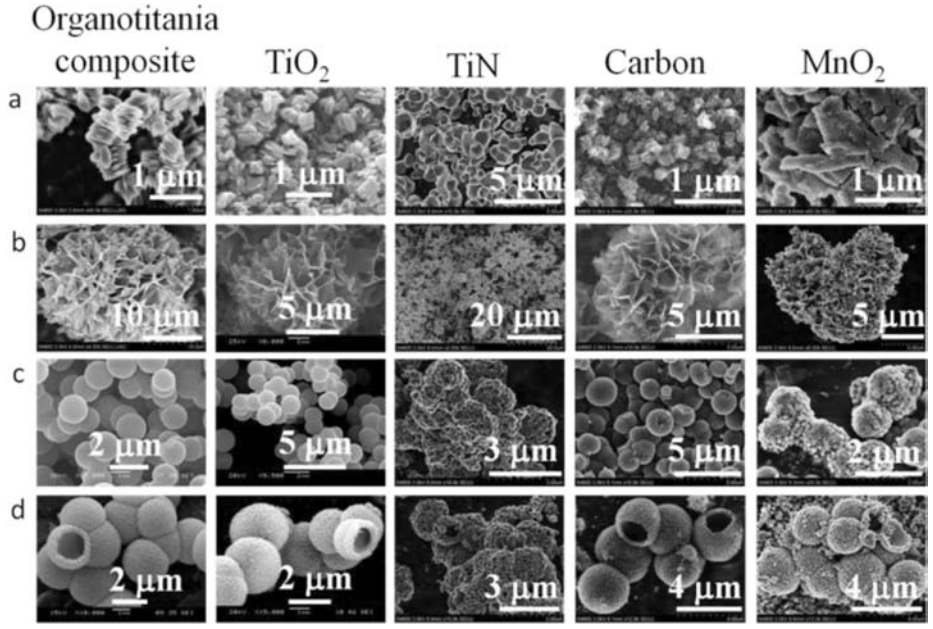

Figure 4. SEM images showing replicated conversions of other morphologies of organotitania composites, TiO_2, TiN, carbon and MnO_2: (a) nanotechtons; (b) flowerlike particles; (c) solid spheres; (d) hollow spheres.

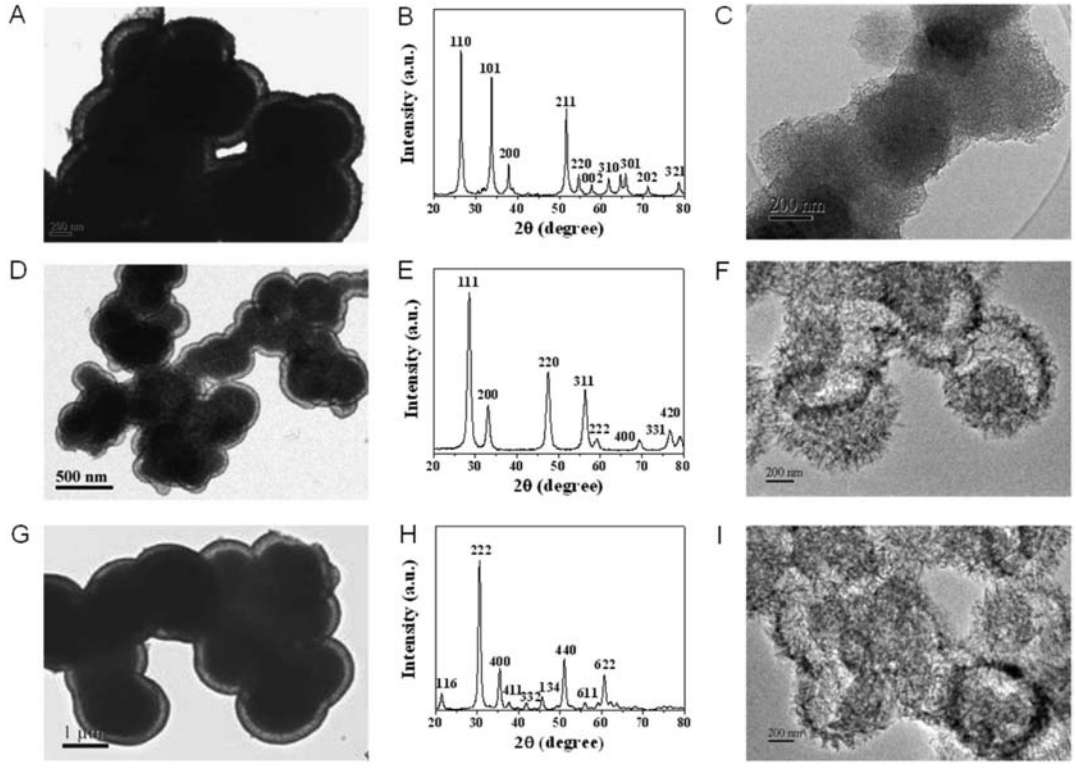

Figure 5. (A, D, G) TEM images and (B, D, H) XRD patterns of (A, B) CeO_2, (D, E) SnO_2, and (G, H) In_2O_3 in yolk−shell spheres obtained by calcinations of the corresponding metal−organic composites in air at 823 K. (XRD sources: SnO_2, JCPDS no. 41-1445; CeO_2, JCPDS no. 34-0394; In_2O_3, JCPDS no. 65-3170). (C, F, I) TEM images of replicated conversions of (C) cerium, (F) tin, and (I) indium into carbon.

The mesoporous structure and high surface area (Table S4) are due to the removal of TiO_2 nanoparticles, as seen in the nitrogen sorption curve analysis (Figure 3d). The thermogravimetric analysis (Figure S14) showed 99.5% weight loss, implying that TiO_2 was completely removed by H_2SO_4 etching. Furthermore, oxidation of the yolk−shell carbon by $KMnO_4$ results in MnO_2 with the replicated structure (step VI in Figure 2). The presence of MnO_2 was further confirmed by the XRD pattern (Figure S15).[33]

The TiO_2, TiN, graphitized carbon, and MnO_2 in solid spheres, nanotechtons, flowerlike particles, and hollow spheres can also be obtained from organotitania composites by using a replicated conversion process (Figure 4). These samples also display mesoporous structures and high Brunauer−Emmett−

dx.doi.org/10.1021/ja210270m | J. Am. Chem.Soc. 2012, 134, 2325−2331

Teller (BET) specific surface areas (S_{BET}),[34] pore volumes (V_P), and pore size distributions (D_P) (see Table S4) resulting from the removal of TiO_2 or organic species. The generality of this approach allows many arbitrary morphologies of organo-titania composites to be transformed into TiO_2, TiN, graphitized carbon, and MnO_2 materials. Furthermore, we demonstrate that the strategy can be extended to other metal–organic composites involving Fe, Ni, Zr, In, Sn, and Ce ions via solvothermal alcoholysis. For example, Figure 5 displays yolk–shell structures for oxides of Ce, Sn, and In. These can also be transformed into metal oxides with replicated structures by calcinations in air (Figures 5 and 6 and Figure S16). Moreover,

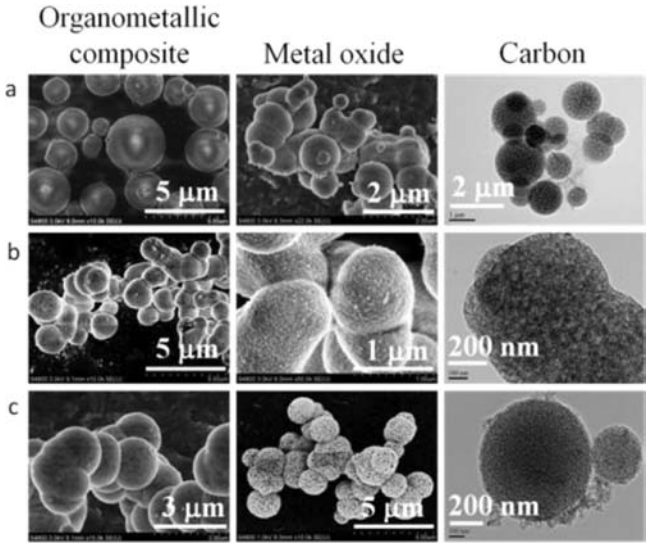

Figure 6. SEM images of replicated conversions of metal–organic composites, metal oxides, and carbon: (a) nickel; (b) zirconium; (c) iron.

the removal of the inorganic framework provides access to carbon-based materials that maintain the structure of the metal–organic composite (Figures 5 and 6). For example, VN solid spheres can be obtained by calcination of the corresponding organovanadium composite under N_2 at 1173 K as well (Figure S17). The temperature was lower for the titanium precursor because it is more active than the other metal precursors. These studies demonstrate the generality of the strategy presented here.

The resulting yolk–shell sphere nanomaterials have superior properties in comparison with those of solid spheres and other nanostructures. For example, Figure 7 shows the photocatalytic activities of TiO_2 and the electric capacitances of carbon in tunable structures (see the Supporting Information for experimental details).[25,35] The TiO_2 in yolk–shell spheres exhibits higher photoactivity than the TiO_2 in solid spheres, flowerlike particles, nanotechtons, and even the crushed yolk–shell spheres. The increased activity may result from the multiple light reflections within the chamber (see the model in Figure S18),[25] taking into account the similar crystallinity of anatase (see the XRD patterns in Figure S19) and the S_{BET}, V_P, and D_P values (see Table S4).[36] This could also account for the higher H_2 yield of TiN in yolk–shell spheres during photocatalytic water splitting in comparison with either TiN in solid spheres or TiN in crushed yolk–shell spheres (see Table S5).[37]

Similarly, the carbon in yolk–shell spheres also exhibits higher electric capacitance than that of other carbon samples, especially the activated carbon commonly employed as the basic electrode material for capacitors because of its extremely high surface area (2071 m^2/g).[35] We posit that the high capacitance is due to the chamber that can provide a reservoir to buffer the ions and minimize the diffusion distance to the interior surfaces.[38,39] The effect of the diffusion process on the electric capacitance was further examined by changing the scanning rates (Figure 8). With increased scanning rates, all of the as-prepared carbon samples display almost constant electric capacitances because of the high graphitization and the mesoporous channels,[40] thus facilitating the electron transport and ion diffusion. However, the activated carbon exhibits a rapid decrease in electric capacitance with increased scanning rate due to the amorphous carbon and the microporous structure, which retard the electron transport and ion diffusion, especially at very high scanning rates.

■ CONCLUSION

Driven by the dearth of strategies for the facile fabrication of structurally and functionally diverse nanomaterials and their increasing applications, we have developed a general approach for the preparation of metal–organic composites with tunable structures via solvothermal alcoholysis. The metal–organic

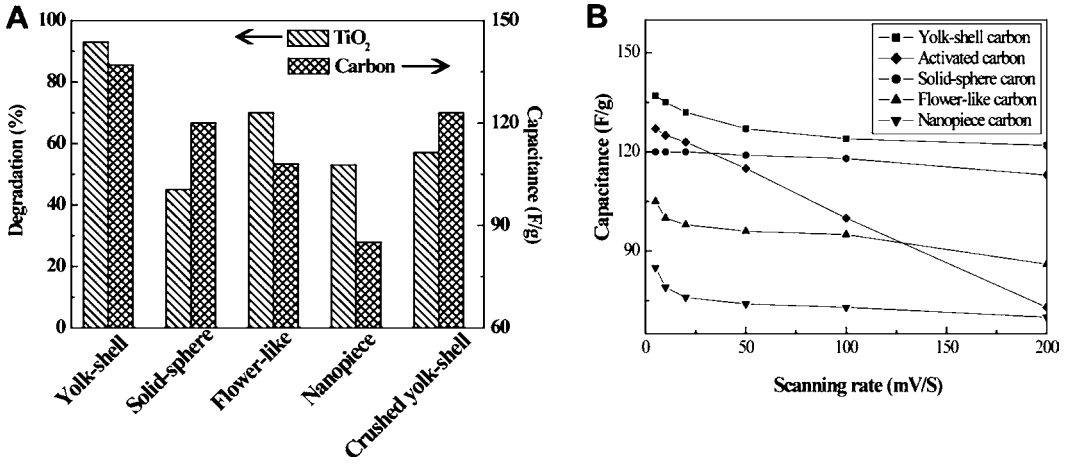

Figure 7. Photocatalytic activities of TiO_2 and electric capacitances of carbon. (A) Effect of the material morphology. (B) Effect of the scanning rate.

dx.doi.org/10.1021/ja210270m | J. Am. Chem.Soc. 2012, 134, 2325–2331

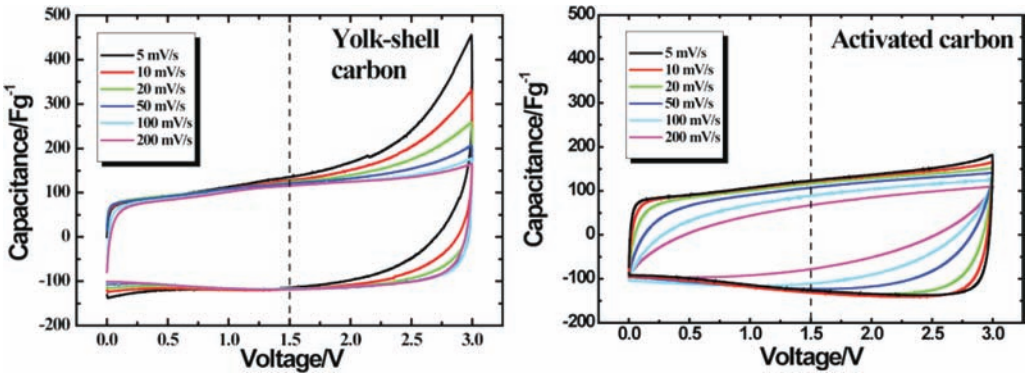

Figure 8. Cyclic voltammograms of carbon capacitors at different scanning rates in 1 M $(C_2H_5)_4NBF_4$/PC electrolyte.

composites can be conveniently converted into structurally and functionally diverse metal oxides, metal nitrides, and graphitized carbon through multitemplating. We therefore expect that the general strategy and design principles described in this study will open new avenues in developing novel materials with enhanced properties for a wealth of applications.

■ ASSOCIATED CONTENT

Supporting Information

Methods for sample preparation, characterization, photodegradation tests, and electrochemical measurements and Figures S1–S22 and Tables S1–S6. This material is available free of charge via the Internet at http://pubs.acs.org.

■ AUTHOR INFORMATION

Corresponding Author

cn37@columbia.edu; Hexing-li@shnu.edu.cn

■ ACKNOWLEDGMENTS

This material is based upon work supported by the National Natural Science Foundation of China (20825724) and the Shanghai Government (10dj1400100, 08GG13) and as part of the Center for Re-Defining Photovoltaic Efficiency through Molecular-Scale Control, an Energy Frontier Research Center funded by the U.S. Department of Energy, Office of Science, Office of Basic Energy Sciences under Award DE-SC0001085.

■ REFERENCES

(1) Zheng, Y. M.; Bai, H.; Huang, Z.; Tian, X.; Nie, F.-Q.; Zhao, Y.; Zhai, J.; Jiang, L. *Nature* **2010**, *463*, 640–643.
(2) Douglas, T. A. *Science* **2003**, *299*, 1192–1193.
(3) Davis, M. E. *Nature* **2002**, *417*, 813–821.
(4) Lu, A. H.; Schuth, F. *Adv. Mater.* **2006**, *18*, 1793–1805.
(5) Joo, S. H.; Choi, S. J.; Oh, I.; Kwak, J.; Liu, Z.; Terasaki, O.; Ryoo, R. *Nature* **2001**, *412*, 169–172.
(6) Barth, J. V.; Costantini, G.; Kern, K. *Nature* **2005**, *437*, 671–679.
(7) Son, Y. W.; Cohen, M. L.; Louie, S. G. *Nature* **2006**, *444*, 347–349.
(8) Tian, B. Z.; Zheng, X.; Kempa, T. J.; Fang, Y.; Yu, N.; Yu, G.; Huang, J.; Lieber, C. M. *Nature* **2007**, *449*, 885–888.
(9) Mann, S. *Nat. Mater.* **2009**, *8*, 781–792.
(10) Zhao, Y.; Thorkelsson, K.; Mastoianni, A. J.; Schilling, T.; Luther, J. M.; Rancatore, B. J.; Matsunaga, K.; Jinnai, H.; Wu, Y.; Poulsen, D.; Fréchet, J. M. J.; Alivisatos, A. P.; Xu, T. *Nat. Mater.* **2009**, *8*, 979–985.
(11) Lim, B.; Jiang, M.; Camargo, P. H. C.; Cho, E. C.; Tao, J.; Lu, X.; Zhu, Y.; Xia, Y. *Science* **2009**, *324*, 1302–1305.
(12) Yang, P. D.; Zhao, D. Y.; Margolese, D. I.; Chmelka, B. F.; Stucky, G. D. *Nature* **1998**, *396*, 152–155.
(13) Douglas, S. M.; Dietz, H.; Liedl, T.; Högberg, B.; Graf, F.; Shih, W. M. *Nature* **2009**, *459*, 414–418.
(14) Lin, Y.; Böker, A.; He, J.; Sill, K.; Xiang, H.; Abetz, C.; Li, X.; Wang, J.; Emrick, T.; Long, S.; Wang, Q.; Balazs, A.; Russell, T. P. *Nature* **2005**, *434*, 55–59.
(15) Park, S.; Lim, J. H.; Chung, S. W.; Mirkin, C. A. *Science* **2004**, *303*, 348–351.
(16) Bao, Z.; Weatherspoon, M. R.; Shian, S.; Cai, Y.; Graham, P. D.; Allan, S. M.; Ahmad, G.; Dickerson, M. B.; Church, B. C.; Kang, Z.; Abernathy, H. W.; Summers, C. J.; Liu, M.; Sandhage, K. H. *Nature* **2007**, *446*, 172–175.
(17) Garnweitner, G.; Niederberger, M. *J. Mater. Chem.* **2008**, *18*, 1171–1182.
(18) Pinna, N. *J. Mater. Chem.* **2007**, *17*, 2769–2774.
(19) Pinna, N.; Niederberger, M. *Angew. Chem., Int. Ed.* **2008**, *47*, 5292–5304.
(20) Park, H. K.; Kim, D. K.; Kim, C. H. *J. Am. Ceram. Soc.* **1997**, *80*, 743–749.
(21) Dai, Z. R.; Pan, Z. W.; Wang, Z. L. *J. Phys. Chem. B* **2002**, *106*, 902–904.
(22) Liu, J. P.; Huang, X.; Li, Y.; Sulieman, K. M.; He, X.; Sun, F. *Cryst. Growth Des.* **2006**, *6*, 1690–1696.
(23) Jian, B. Y.; Zhao, X. P. *J. Colloid Interface Sci.* **2003**, *57*, 228–236.
(24) Yin, Y.; Rioux, R. M.; Erdonmez, C. K.; Hughes, S.; Somorjai, G. A.; Alivisatos, A. P. *Science* **2004**, *30*, 711–714.
(25) Li, H.; Bian, Z.; Zhu, J.; Zhang, D.; Li, G.; Huo, Y.; Li, H.; Lu, Y. *J. Am. Chem. Soc.* **2007**, *129*, 8406–8407.
(26) Shaviv, R. *Mater. Sci. Eng., A* **1996**, *209*, 345–352.
(27) Fischer, A.; Jun, Y.; Thomas, A.; Antonietti, M. *Chem. Mater.* **2008**, *20*, 7383–7389.
(28) Yang, H. F.; Yan, Y.; Liu, Y.; Zhang, F.; Zhang, R.; Meng, Y.; Li, M.; Xie, S.; Tu, B.; Zhao, D. *J. Phys. Chem. B* **2004**, *108*, 17320–17328.
(29) Yoon, S. B. *J. Am. Chem. Soc.* **2005**, *127*, 4188–4189.
(30) Maldonado-Hódar, F. J.; Moreno-Castilla, C.; Rivera-Utrilla, J.; Hanzawa, Y.; Yamada, Y. *Langmuir* **2000**, *16*, 4367–4373.
(31) Zhang, L.; Fu, H.; Zhu, Y. *Adv. Funct. Mater.* **2008**, *18*, 2180–2189.
(32) Maldonado-Hódar, F. J.; Ferro-Garcia, M. A.; Rivera-Utrilla, J.; Moreno-Castilla, C. *Carbon* **1999**, *37*, 1199–1205.
(33) Zhu, H. T.; Luo, J.; Yang, H. X.; Liang, J. K.; Rao, G. H.; Li, J. B.; Du, Z. M. *J. Phys. Chem. C* **2008**, *112*, 17089–17094.
(34) The BET method was utilized to calculate S_{BET} using adsorption data in a relative pressure range from 0.05 to 0.3.
(35) Liu, H. J.; Cui, W. J.; Jin, L. H.; Wang, C. X.; Xia, Y. Y. *J. Mater. Chem.* **2009**, *19*, 3661–3667.
(36) The yolk–shell and solid spherical carbon and TiN exhibited similar S_{BET} values since they were obtained from the titanium–organic composites after being treated at very high temperature (1273 or 1573 K), causing the collapse of the most of the small-sized porous structures (Figure S20).
(37) We found that grinding the yolk–shell TiO_2 gave a 57% decrease in the activity, which was similar to that of the solid spheres

(see Figure 7), though the surface area of the ground yolk–shell TiO_2 slightly increased from 62 to 68 m^2/g (Table S4). This implies that the photocatalytic activity depends on the yolk–shell structure rather than on the surface area.

(38) Wang, D. W.; Li, F.; Liu, M.; Lu, G. Q.; Cheng, H. M. *Angew. Chem., Int. Ed.* **2008**, *47*, 373–376.

(39) Fang, B.; Kim, M.; Kim, J. H.; Yu, J. S. *Langmuir* **2008**, *24*, 12068–12072.

(40) Support for the formation of mesopourous graphitized carbon with high surface area is shown in Table S6 and in the TEM images and N_2 adsorption–desorption isotherms in Figures S21 and S22.